Evaluation of spin mixing conductance in $Co_2FeGa_{0.5}Ge_{0.5}$/Pt bilayer and the effect of ultrathin Cu, Ni, Ru, Ta, or Cr insertion layers

Madhav M. Bhat[1,2], H. Suto[2,*], T. T. Sasaki[2], A. Perumal[1], A. Srinivasan[1,*], Y. Sakuraba[1,2,3]

[1]Department of Physics, Indian Institute of Technology Guwahati, Guwahati-781039, India.

[2] Research Center for Magnetic and Spintronic Materials, NIMS, Tsukuba, 305-0047, Japan.

[3]Graduate School of Pure and Applied Sciences, University of Tsukuba, Tsukuba, 305-8571, Japan.

Email: *SUTO.Hirofumi@nims.go.jp, *asrini@iitg.ac.in

ABSTRACT

Improving the spin mixing conductance at the ferromagnet/heavy metal (FM/HM) interface with a low Gilbert damping constant in the FM layer is a key requirement for developing efficient spintronic devices. To evaluate the potential of $Co_2FeGa_{0.5}Ge_{0.5}$ as the FM layers in such structures, epitaxial $Co_2FeGa_{0.5}Ge_{0.5}$ single-layer and $Co_2FeGa_{0.5}Ge_{0.5}$/Pt bilayer films were deposited on MgO substrate using magnetron sputtering, and their Gilbert damping constants were evaluated from ferromagnetic resonance spectra. While the single-layer samples exhibit a low damping constant of ~ 1.07×10^{-3}, an enhancement in the damping constant was observed in the bilayer samples due to spin pumping across the $Co_2FeGa_{0.5}Ge_{0.5}$/Pt interface, from which relatively large spin mixing conductance ($g_{\mathrm{eff}}^{\uparrow\downarrow}$) of $(2.78\pm0.09)\times10^{19}$ m^{-2} was evaluated. Further, to investigate the effect of interface property on $g_{\mathrm{eff}}^{\uparrow\downarrow}$, ultrathin (~ 0.2 nm) Cu, Ni, Ru, Ta, or Cr insertion layers were introduced between the $Co_2FeGa_{0.5}Ge_{0.5}$ and Pt. Inserting a non-magnetic (NM) Cu layer results in a pronounced decrease of $g_{\mathrm{eff}}^{\uparrow\downarrow}$, whereas the FM Ni layer leaves $g_{\mathrm{eff}}^{\uparrow\downarrow}$ nearly unchanged. In the case of Ru and Ta insertion layers, a modest reduction in $g_{\mathrm{eff}}^{\uparrow\downarrow}$ is observed despite their NM nature. The antiferromagnetic Cr insertion layer also causes a small decrease in $g_{\mathrm{eff}}^{\uparrow\downarrow}$. The observed change in $g_{\mathrm{eff}}^{\uparrow\downarrow}$ depends on the insertion material, indicating that their physical properties, such as magnetic, non-magnetic, antiferromagnetic, light or heavy metal, reflect on $g_{\mathrm{eff}}^{\uparrow\downarrow}$.

1. INTRODUCTION

The development of high-performance non-volatile magnetoresistive random access memory requires a magnetic tunnel junction with energy-efficient switching of magnetization in the active ferromagnetic (FM) layer [1]. This favours the adoption of the spin-orbit torque (SOT) mechanism, where spin current injection occurs from a nonmagnetic (NM) layer to the active FM layer [2,3]. In this switching scheme, spin mixing conductance ($g_{\text{eff}}^{\uparrow\downarrow}$) is a key parameter to quantify the spin current from the NM to the FM layer. So, an FM/NM interface with high $g_{\text{eff}}^{\uparrow\downarrow}$ (~ 10^{19} to 10^{20} m^{-2}) is essential for improving the SOT efficiency [4–6].

The value of $g_{\text{eff}}^{\uparrow\downarrow}$ is influenced by several key properties of the FM/NM interface. First-principles studies by Barati *et al*. [7] show that the Gilbert damping constant (α) is largely affected by the interfacial electronic structure, spin-orbit coupling strength of the NM layer, and the thicknesses of the FM and NM layers, which together determine $g_{\text{eff}}^{\uparrow\downarrow}$. This dependence is experimentally illustrated by Azzawi *et al*. [8] in Co/Pt, Co/Au, and $Ni_{81}Fe_{19}$/Pt bilayers. Zhang *et al*. [9] theoretically showed that an increase in interface roughness enhanced $g_{\text{eff}}^{\uparrow\downarrow}$ in the permalloy/Pt bilayer sample. Tokaç *et al*. [10] experimentally observed the effect of FM and NM crystal structures at the interface in Ta/Cu/Co/Cu (or Ir)/Ta multilayers and found that $g_{\text{eff}}^{\uparrow\downarrow}$ is enhanced when the FM layer and NM overlayers have the same crystal structure. Other studies have also explored the impact of insertion layers at the FM/NM interface on $g_{\text{eff}}^{\uparrow\downarrow}$. For example, Kumar *et al*. [5] studied the effect of Cu insertion layer (0 – 10 nm) on $g_{\text{eff}}^{\uparrow\downarrow}$ in Co_2FeAl/β-Ta bilayer, and Swindells *et al*. [11,12] examined the effect of Au insertion layer (0 – 3 nm) in $Co_{25}Fe_{75}$/Pt and $Ni_{80}Fe_{20}$/Pt bilayers. These studies have provided valuable insights into the roles of proximity-induced magnetization and interface spin current transparency in modifying $g_{\text{eff}}^{\uparrow\downarrow}$. Considering these studies, a need for a detailed structural analysis of the NM overlayer at the FM/NM interface is desired to separate the effects of insertion layers from the changes in the NM layer structure that the insertion layers may induce.

Another crucial parameter for energy-efficient switching is a low α of the active FM layer [13]. Since α is proportional to the total density of states (DOS) at the Fermi level (E_F), half-metallic materials can exhibit low α due to the presence of only one type of electronic spin in DOS at E_F [14–16]. Additionally, suppression of spin-flip scattering in half-metals further decreases α [17]. Half-metallicity is also beneficial for achieving large magnetoresistance output [18–21]. In these respects, Co_2Fe-based $Co_2FeGa_{0.5}Ge_{0.5}$ (CFGG) Heusler alloy has gathered considerable attention with the illustration of enhanced magnetoresistance ratio in current-perpendicular-to-plane (CPP) giant magnetoresistance (GMR) device [18,22,23] with a α of ~ 0.008 [24]. Regarding the NM layer, heavy metals (HMs) such as Pt, Ta, W, Ir, or Hf have been reported as an effective spin-current source. Such materials have a high spin Hall angle (θ_H) arising from large spin-orbit coupling (SOC), since SOC scales with the atomic number (Z) as a function of Z^4 [25,26].

Based on the above material considerations, this study focuses on the CFGG/Pt system and investigates its $g_{\text{eff}}^{\uparrow\downarrow}$. The CFGG single-layer and CFGG/Pt bilayer samples were grown epitaxially on MgO substrates, and their α was evaluated using the ferromagnetic resonance (FMR) technique. The enhanced damping in the bilayer CFGG/Pt sample signifies spin pumping across the CFGG/Pt interface, from which relatively high $g_{\text{eff}}^{\uparrow\downarrow}$ value of $(2.78\pm0.09)\times10^{19}$ m^{-2} was estimated. The effect of ultrathin insertion layers on $g_{\text{eff}}^{\uparrow\downarrow}$ was further examined, highlighting the material-dependent variations in $g_{\text{eff}}^{\uparrow\downarrow}$. Notably, structural analysis using X-ray diffraction (XRD) and scanning transmission electron microscope (STEM) analysis confirmed that the Pt layer structure was unaffected by the insertion layers, which excluded the possible contributions to the change in $g_{\text{eff}}^{\uparrow\downarrow}$ from structural modifications in the Pt layer. The change in $g_{\text{eff}}^{\uparrow\downarrow}$ was found to depend on the insertion material, indicating that their physical properties, such as magnetic, nonmagnetic, antiferromagnetic, light or heavy metal, are reflected in $g_{\text{eff}}^{\uparrow\downarrow}$.

2. EXPERIMENTAL DETAILS

Figures 1(a)–1(c) illustrate the schematic structure of the samples used in this study, *viz*., CFGG (7.5, 8.8, 10.5, 12.5, 14, 16.3, and 18.5 nm) single-layer samples, CFGG (7.5, 8.8, 10.5, 12.5, 14, 16.3, and 18.5 nm)/Pt (10 nm) and CFGG (14 nm)/Pt (0.5, 1, 2, 3, 5, and 10 nm) bilayer samples, and CFGG (7.5 nm)/X (~ 0.2 nm)/Pt (10 nm) bilayer samples with insertion of X (Cu, Ni, Ru, Ta, or Cr) layers. All the samples were deposited on MgO (001) substrate at ambient temperature using an ultra-high vacuum magnetron sputtering system with a base pressure of ~ 10^{-7} Pa. Prior to the deposition, substrates were cleaned with acetone, propanol, and deionized water, followed by *in situ* argon ion milling. The CFGG layers were deposited from an alloy target of $Co_{1.95}Fe_{0.89}Ga_{0.48}Ge_{0.68}$ and subsequently annealed *in situ* at 600 °C for 30 minutes to enhance the atomic ordering. The composition of the CFGG layer was determined to be

$Co_{2.06\pm0.01}Fe_{0.99\pm0.01}Ga_{0.53\pm0.01}Ge_{0.42\pm0.01}$ by X-ray fluorescence spectroscopy. For the single-layer samples, a 2 nm Al capping layer was deposited to avoid oxidation (not shown in Fig. 1(a)) of the CFGG layer. In the bilayer samples, a Pt layer was deposited on the CFGG layer after cooling down to room temperature, which served as both a spin sink and a capping layer. For the bilayer samples with an insertion layer, ~ 0.2 nm thick layer of Cu, Ni, Ru, Ta, or Cr was deposited on the CFGG layer at room temperature before the deposition of the Pt layer. The detailed deposition parameters and purity of the sputtering sources are given in Table 1.

Table 1: Deposition parameters and purity of sputtering sources.

Material	Target purity and supplier	Power source	Power (W)	Ar flow rate (sccm)	Pressure (mTorr)	Deposition rate (Å/s)
CFGG	99.9% Toshima Manufacturing Co., Ltd.	RF	90	50	1.5	0.20
Pt	99.99% Tanaka Precious Metal Technologies Co., Ltd.	DC	50	100	4.2	0.54
Cu	99.99% Kojundo Chemical Laboratory Co.,Ltd.	RF	20	10	8	0.18
Ni	99.99% Toshima Manufacturing Co., Ltd.	DC	30	30	5.5	0.08
Ru	99.9% Toshima Manufacturing Co., Ltd.	RF	30	15	4.5	0.08
Ta	99.99% Toshima Manufacturing Co., Ltd.	RF	30	10	5	0.12
Cr	99.99% Toshima Manufacturing Co., Ltd.	RF	50	50	7.5	0.04

The film thickness and interfacial roughness were determined by X-ray reflectivity measurements. A model consisting of CFGG and Pt layers was used to fit the XRR data of CFGG/Pt and

CFGG/X/Pt (X = Cu, Ni, Ru, Ta, or Cr) samples. The evaluated interfacial roughness values are listed in Table 2.

Table 2: Interfacial roughness at the CFGG and Pt interface in CFGG/Pt and CFGG/X/Pt (X = Cu, Ni, Ru, Ta, or Cr) samples.

	CFGG/Pt	CFGG/Cu/Pt	CFGG/Ni/Pt	CFGG/Ru/Pt	CFGG/Ta/Pt	CFGG/Cr/Pt
Interface roughness (nm)	~ 0.3	~ 0.5	~ 0.5	~ 0.5	~ 0.4	~ 0.5

The structure of the samples was analyzed by XRD with Cu-K_α radiation (λ = 1.5406 Å) and cross-sectional (S)TEM analysis (FEI Titan G2 80-200). The specimens for the STEM analysis were fabricated by a standard lift-out method using focused ion-beam/scanning electron microscope (FIB/SEM), FEI Helios G4.

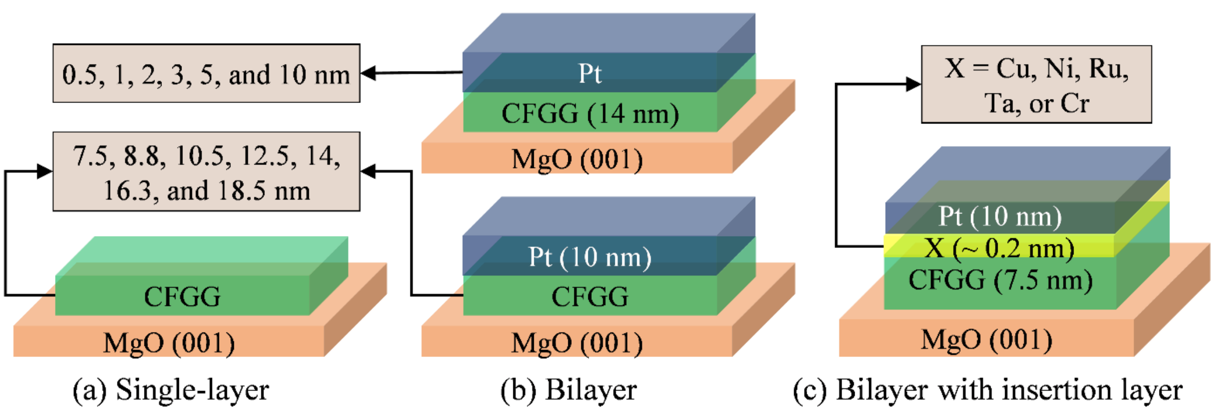

Fig. 1. Schematic representation of the thin film stack of the (a) CFGG (7.5, 8.8, 10.5, 12.5, 14, 16.3, and 18.5 nm) single-layer, (b) CFGG (7.5, 8.8, 10.5, 12.5, 14, 16.3, and 18.5 nm)/Pt (10 nm) and CFGG (14 nm)/Pt (0.5, 1, 2, 3, 5, and 10 nm) bilayer, and (c) CFGG (7.5 nm)/X (~ 0.2 nm)/Pt (10 nm) bilayer with insertion layer, deposited on the MgO (001) substrate.

To evaluate $g_{\mathrm{eff}}^{\uparrow\downarrow}$, α of each sample was determined using in-plane broadband FMR spectra recorded in the frequency range of 16 GHz to 36 GHz using an FMR spectrometer (Phase FMR – 40) unit attached to the physical property measurement system (PPMS, Quantum Design, USA). During the measurement, lock-in detection technique was employed to improve the signal-to-noise ratio, which requires a reference a.c. signal to lock on. This signal was generated by a set of Helmholtz coils powered by an alternating current source, producing a small (~ 1 Oe) modulation field. The obtained FMR spectra were fitted with the equation [5],

$$\frac{dI}{dH} = K_1 \frac{[(\Delta H/2)^2 - (H - H_\mathrm{r})^2]}{[(\Delta H/2)^2 + (H - H_\mathrm{r})^2]^2} + K_2 \frac{2(H - H_\mathrm{r})(\Delta H/2)}{[(\Delta H/2)^2 + (H - H_\mathrm{r})^2]^2}. \qquad (1)$$

Here, dI/dH is the derivative of the microwave absorption signal with respect to the applied external magnetic field (H). K_1 and K_2 are coefficients that correspond to the symmetric and antisymmetric components of the FMR spectrum, respectively. This fitting provides the resonance field ($\mu_0 H_\mathrm{r}$) and the linewidth ($\mu_0 \Delta H$) of the FMR spectrum, from which α is calculated. The total α (α_total) obtained from the experiments contains both intrinsic (α_int) and extrinsic (α_ext) components, and α_ext consists of contributions from spin pumping (α_sp), two-magnon scattering, radiative damping, and eddy current [27]. Among these contributions, the dominant one from the additional Pt layer increases α_sp by spin pumping. Therefore, the enhancement in α_total of the bilayer samples from the single-layer samples ($\Delta\alpha$) can be expressed as follows [4]:

$$\Delta\alpha = \alpha_\mathrm{Bilayer} - \alpha_\mathrm{Single-layer} \cong \alpha_\mathrm{sp}. \qquad (2)$$

Then, $g_\mathrm{eff}^{\uparrow\downarrow}$ is evaluated using the relation [4],

$$\Delta\alpha = \frac{g\mu_\mathrm{B}}{4\pi M_\mathrm{s}} \frac{1}{t_\mathrm{CFGG}} g_\mathrm{eff}^{\uparrow\downarrow}, \qquad (3)$$

where, g, μ_B, M_s, and t_CFGG refer to Lande's g factor, Bohr magneton, saturation magnetization, and thickness of the CFGG layer, respectively. Note that, $g_\mathrm{eff}^{\uparrow\downarrow}$ varies with the Pt layer thickness because of the contribution due to spin back flow from the Pt to the CFGG layer.

3. RESULTS AND DISCUSSION

3.1. Structural analysis

Figures 2(a) and 2(b) show the 2θ-ω XRD patterns of CFGG single-layer samples with a thickness (t_CFGG) of 7.5, 12.5, and 18.5 nm, along the out-of-plane direction for $\chi = 0°$ and the <111> direction for $\chi = 54.7°$, respectively. The corresponding results of CFGG (t_CFGG)/Pt (10 nm) bilayer samples are shown in Figs. 2(c) and 2(d), respectively. In all the samples, the observed peaks of CFGG 004 and Pt 002 for $\chi = 0°$ confirm epitaxial growth along the [001] direction. Additionally, the presence of CFGG 002 and 111 superlattice peaks confirm the $L2_1$-type ordered crystal structure. Due to the similar atomic scattering factors of Co and Fe, standard XRD techniques are limited in their ability to detect Co-Fe disorder. Nonetheless, such disorder is expected to be suppressed as a result of the high annealing temperature of 600 °C used, which was confirmed through the anomalous XRD technique using synchrotron-radiated X-ray in an earlier study [28].

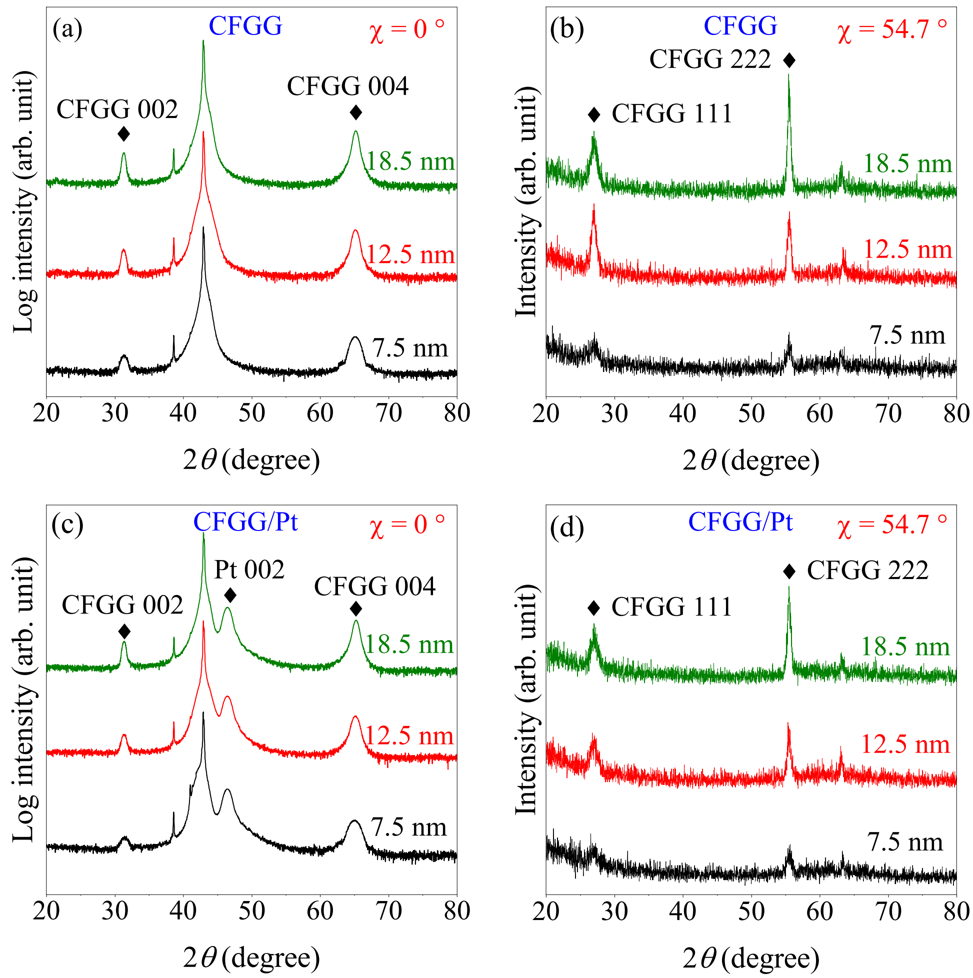

Fig. 2. XRD patterns of 2θ-ω scans for CFGG (7.5, 12.5, and 18.5 nm) single-layer samples for (a) $\chi = 0°$ and (b) $\chi = 54.7°$. (c, d) Corresponding results for CFGG (7.5, 12.5, and 18.5 nm)/Pt (10 nm) bilayers.

3.2. Evaluation of spin mixing conductance across the CFGG/Pt interface

To assess $g_{\mathrm{eff}}^{\uparrow\downarrow}$ and examine its dependence on the CFGG/Pt interface, α_{total} of all samples were evaluated using FMR measurements. Figure 3(a) shows a typical FMR spectrum along with the fitted curve based on Eq. (1), from which $\mu_0 H_{\mathrm{r}}$ and $\mu_0 \Delta H$ were extracted. Figure 3(b) shows the variation of the evaluated $\mu_0 H_{\mathrm{r}}$ as a function of the resonance frequency (f_{r}), which is fitted with the Kittel's equation [6] to evaluate the gyromagnetic ratio (γ). This γ value of 1.81×10^{11} rad/s/T is then used to calculate α_{total} by fitting $\mu_0 \Delta H$ *versus* f_{r} shown in Fig. 3(c), using the equation [6],

$$\mu_0 \Delta H = \frac{4\pi\alpha_{\mathrm{total}}}{\gamma} f_{\mathrm{r}} + \mu_0 \Delta H_0. \quad (4)$$

Here, $\mu_0\Delta H_0$ corresponds to the linewidth broadening due to inhomogeneities in the CFGG layer, and α_{total} is the Gilbert damping constant obtained as a fitting parameter.

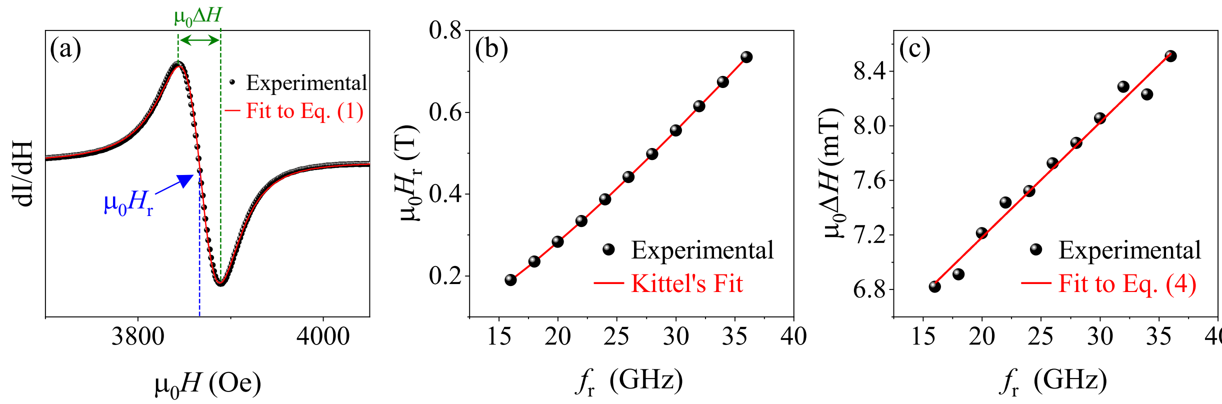

Fig. 3. (a) FMR spectrum of a 14 nm thick CFGG single-layer sample measured at 24 GHz fitted with Eq. (1), (b) $\mu_0 H_r$ *versus* f_r data fitted to the Kittel's equation, and (c) $\mu_0\Delta H$ *versus* f_r plot along with fit to Eq. (4).

Figure 4(a) depicts the variation of α_{total} with t_{CFGG} for both single-layer and bilayer samples. For the single-layer samples, α_{total} remains nearly independent of t_{CFGG} in the thickness range of 18.5–8.8 nm and slightly increases for t_{CFGG} < 8.8 nm. In bilayer samples, α_{total} is significantly increased compared to single-layer samples due to the transfer of spin current from the CFGG layer to the Pt layer. Figure 4(b) shows the t_{CFGG} dependence of the increase in α_{total} ($\Delta\alpha$), which shows a monotonic decrease with increasing t_{CFGG}.

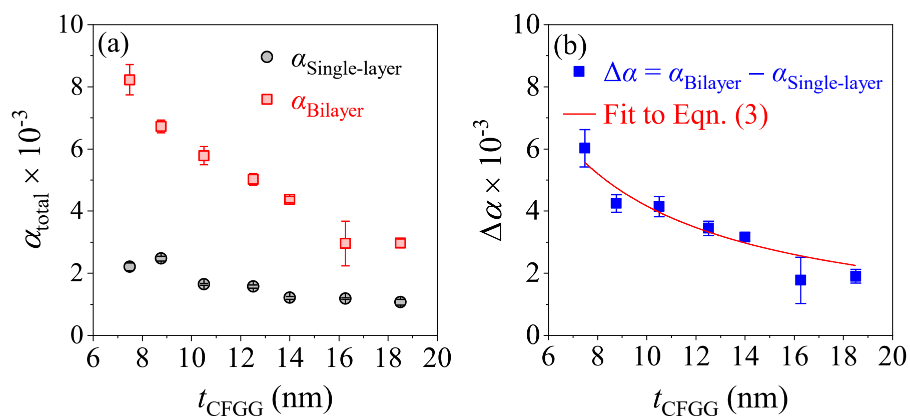

Fig. 4. Variations of (a) α_{total} with a t_{CFGG} in single and bilayer samples, and (b) $\Delta\alpha$ with t_{CFGG}.

By fitting the data in Fig. 4(b) with Eq. (3), $g_{eff}^{\uparrow\downarrow}$ was evaluated to be $(2.78\pm0.09)\times10^{19}$ m^{-2}, which is relatively high in comparison with the previously reported values for conventional FM/Pt bilayer systems such as Co/Pt ($(1.42\pm0.01)\times10^{19}$ m^{-2}), CoFe/Pt ($(2.65\pm0.08)\times10^{19}$ m^{-2}), and Py/Pt

((2.53±0.02)×10^{19} m^{-2}) [29]. In this analysis, the effect of spin back flow is neglected because the Pt layer thickness is sufficiently larger than the reported value of the Pt spin diffusion length [30]. The effect of the Pt layer thickness is discussed below.

Figure 5 represents the variation of $\Delta\alpha$ with the thickness of the Pt layer (t_{Pt}) for the sample consisting of CFGG (14 nm)/Pt (0.5, 1, 2, 3, 5, and 10 nm) layers. One can notice the decrease in $\Delta\alpha$ value in the lower t_{Pt} range (≤ 4 nm). This reduction is attributed to spin current reflection at the Pt/air interface. When the Pt layer thickness is comparable to its spin diffusion length (λ_{Pt}), the reflected spin current flows back into the CFGG layer, thereby reducing $\Delta\alpha$.

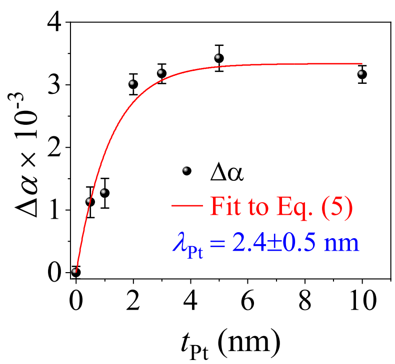

Fig. 5. Variation of $\Delta\alpha$ with Pt layer thickness for the bilayer films with a 14 nm CFGG layer.

As a result, Eq. (3) gets modified to [31],

$$\Delta\alpha = \frac{g\mu_B}{4\pi M_s}\frac{1}{t_{CFGG}}\, g_{eff}^{\uparrow\downarrow}\left(1 - e^{-2t_{Pt}/\lambda_{Pt}}\right). \tag{5}$$

The terms in the bracket on the right side represent spin current reflection at the Pt/air interface, for the case of perfect reflection. Thus, the factor of 2 in the exponential term represents the total distance travelled by the spin current as it returns to the CFGG layer. λ_{Pt} is estimated to be 2.4±0.5 nm from a fit to the data shown in Fig. 5 to Eq. (5). The obtained λ_{Pt} is consistent with the previously reported value of 2.4±0.3 nm [30]. This validates the assumption made in the earlier analysis of $g_{eff}^{\uparrow\downarrow}$ that λ_{Pt} is much smaller than the t_{Pt} of 10 nm. Thus, the estimated $g_{eff}^{\uparrow\downarrow}$ is unaffected by the spin current reflection.

3.3. Effect of various insertion layers on spin mixing conductance

To explore the impact of ultrathin insertion layers on $g_{eff}^{\uparrow\downarrow}$, we introduced ~ 0.2 nm thick Cu, Ni, Ru, Ta, or Cr between the CFGG and Pt layers. In these experiments, t_{CFGG} and t_{Pt} were set to 7.5 nm and 10 nm, respectively, because the α of a thinner CFGG layer is more sensitive to changes in spin-pumping. First, to examine the possible modifications in the Pt structure due to different insertion layers, XRD patterns were recorded. Figures 6(a) and 6(b) show the 2θ-ω scans of CFGG (7.5 nm)/X (~ 0.2 nm)/Pt (10 nm) samples with various insertion layers (X = Cu, Ni, Ru, Ta, or Cr) along the <001> ($\chi = 0°$) and <110> ($\chi = 45°$) directions, respectively. It is to be noted that, in Fig. 6(a), the CFGG 002 peak is not visible. However, for the same 7.5 nm CFGG layer thickness, the CFGG 002 peak is clearly visible in the Figs. 2(a) and 2(c) for the CFGG (7.5 nm) and CFGG (7.5 nm)/Pt (10 nm) films, respectively, when measured using a 0D-mode XRD detector. The reduced intensity of the CFGG 002 peak in Fig. 6(a) is due to the use of a 2D-mode XRD detector, which is employed for rocking curve measurements, as discussed later. The XRD patterns for the samples with an insertion layer are almost identical to that of the bilayer sample. This indicates that the [001]-direction epitaxial growth of CFGG and Pt layers was maintained irrespective of the type of insertion layer, with negligible change in the crystal structure of the CFGG and Pt layers.

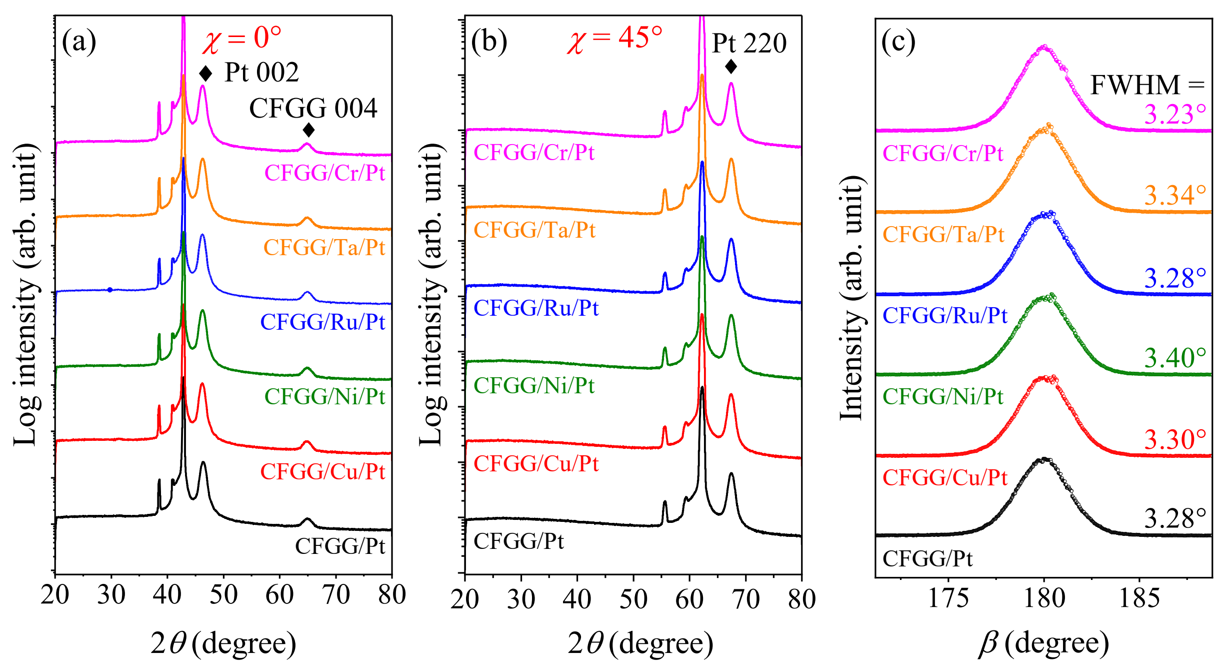

Fig. 6. XRD patterns of CFGG (7.5 nm)/X (~ 0.2 nm)/Pt (10 nm) samples recorded at (a) $\chi = 0°$ and (b) $\chi = 45°$ for X = Cu, Ni, Ru, Ta, or Cr. (c) The corresponding rocking curves recorded about the Pt 220 peak.

To study the structure of the Pt layer in more detail, rocking curve measurement was carried out for the Pt 220 peak, as shown in Fig. 6(c). Pt 220 peak was chosen because of its larger separation from the MgO peak than that in the <001> direction scan. The Pt 220 rocking curves show identical shape and intensity. The full-width at half-maximum (FWHM) values of these peaks for all the samples with different insertion layers are mentioned in Fig. 6(c). The nearly identical FWHM values confirm that the Pt epitaxial layer is not largely influenced by the insertion layers.

Cross-sectional TEM analysis was performed on the CFGG (7.5 nm)/Cu (~ 0.2 nm)/Pt (10 nm) structure. This sample was chosen as a representative sample to confirm the presence of the ultra-thin insertion layer, given that the Cu insertion most significantly modifies $g_{\text{eff}}^{\uparrow\downarrow}$, as discussed later. Figures 7(a) and 7(b) show the cross-sectional high-angle annular dark-field (HAADF)-STEM images, energy dispersive spectroscopy (EDS) elemental maps, and line compositional profiles of Mg, O, Co, Fe, Ga, Ge, Cu, and Pt at low magnification for the CFGG (7.5 nm)/Pt (10 nm) and CFGG (7.5 nm)/Cu (~ 0.2 nm)/Pt (10 nm) samples, respectively.

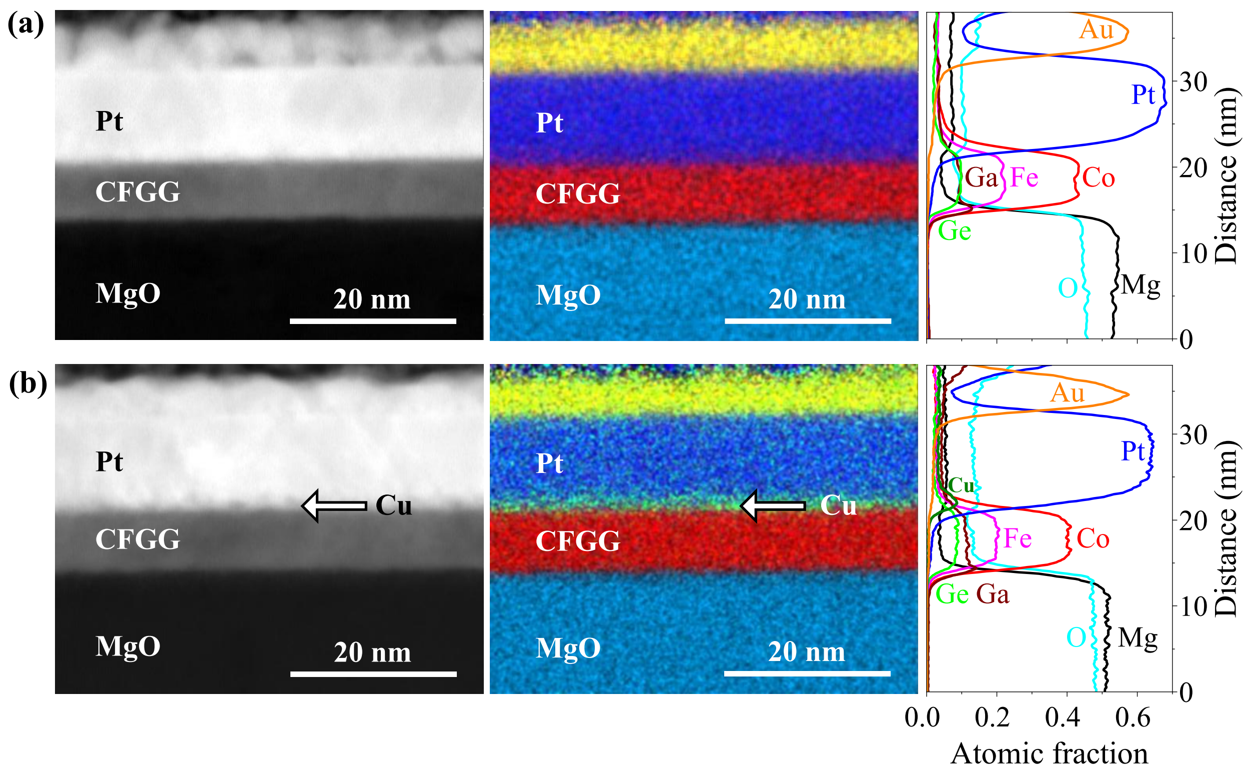

Fig. 7. Cross-sectional HAADF-STEM image and EDS elemental maps of bilayers (a) without Cu insertion layer, and (b) with ~ 0.2 nm Cu insertion layer. (a) and (b) also includes the line compositional profile across the interfaces.

The HAADF-STEM image and EDS elemental map confirm the presence of the Cu insertion layer (indicated by an arrow) at the CFGG/Pt interface, further supported by the line composition profile as depicted in Fig. 7(b). The line compositional profiles in Figs. 7(a) and 7(b) show the oxygen distribution (~ 10-15%) throughout CFGG and Pt layers. The oxygen in these regions is an artifact, resulting from oxygen adhering to the sample surface and contact with the sample being analyzed. To analyze the Cu distribution in detail, a separate EDS elemental map of Cu, and the corresponding multiple EDS line profiles from 5-nm-wide regions, denoted as (i)–(x), are shown in Figs. 8(a) and 8(b), respectively. These results suggest the non-uniformity in the Cu insertion layer. An averaged EDS line profile from the entire region indicated by the red dashed box in Fig. 8(a), is shown in red in Fig. 8(b). A weak Cu signal is additionally detected in the Pt region, which can be attributed to the spectral overlap effects, as the Cu-K and Pt-Lλ peaks are close in energy, at approximately 8.0 keV and 8.26 keV, respectively. This overlap-induced artifact is supported by the fact that the Cu signal inside the Pt layer does not decay with the distance from the interface.

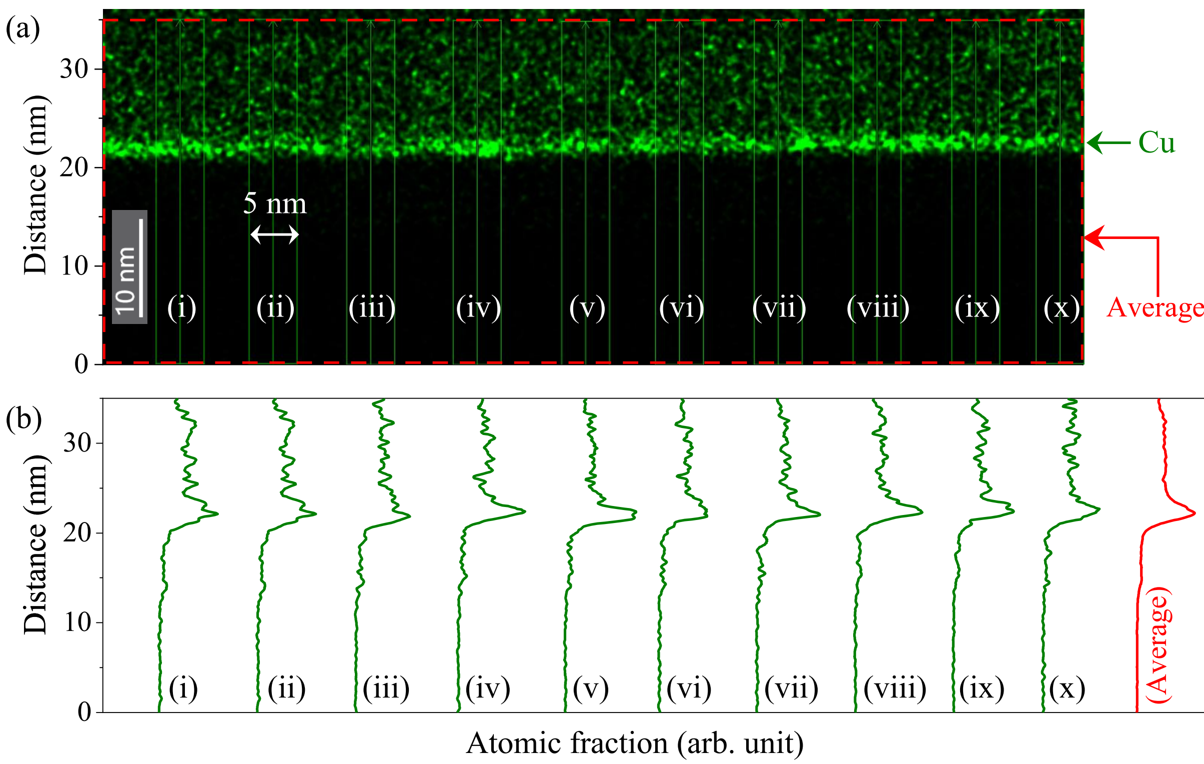

Fig. 8. (a) Cross-sectional EDS elemental map of the Cu insertion layer in CFGG (7.5 nm)/Cu (~ 0.2 nm)/Pt (10 nm) sample, and (b) the corresponding compositional line profiles across the interface at different positions denoted as (i)–(x) in (a).

The high-magnification HAADF-STEM images are shown in Figs. 9(a) and 9(b). The Pt layer grows epitaxially on the CFGG layer regardless of the Cu layer insertion. The orientation relationship between CFGG and Pt layers is described as $(001)_{\mathrm{CFGG}}/(001)_{\mathrm{Pt}}$, $[100]_{\mathrm{CFGG}}/[110]_{\mathrm{Pt}}$. Given that the ultrathin insertion layer is not continuous, some portion of CFGG and Pt remain in direct contact, which can partly explain why the Pt structure is largely unaffected by the deposition of insertion layers.

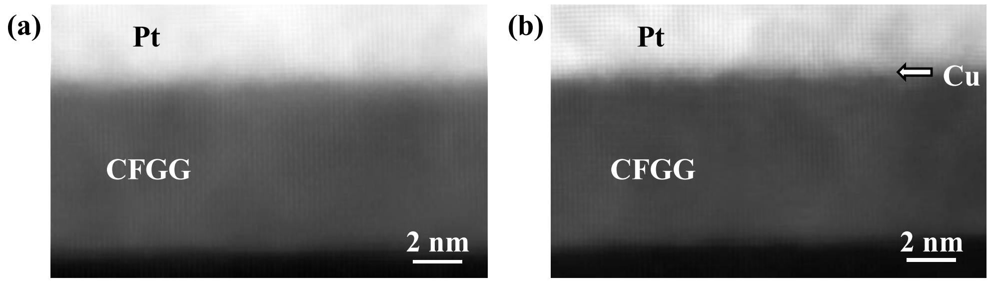

Fig. 9. High-magnification HAADF-STEM images obtained from the samples (a) without Cu insertion layer, and (b) with ~ 0.2 nm Cu insertion layer. The arrow in the figure indicates the position of Cu insertion.

Figures 10(a) and 10(b) show the comparison of α_{total} and $g_{\mathrm{eff}}^{\uparrow\downarrow}$ for the samples without and with insertion layer. The corresponding ratio of change in α_{total} and $g_{\mathrm{eff}}^{\uparrow\downarrow}$ due to different insertion layers are shown in Figs. 10(c) and 10(d), respectively. The change in $g_{\mathrm{eff}}^{\uparrow\downarrow}$ cannot be explained solely by the changes in interface roughness observed for different insertion layers as listed in Table 2. This indicates that intrinsic physical properties of the insertion layers play a dominant role in changes observed in $g_{\mathrm{eff}}^{\uparrow\downarrow}$. The sample without insertion layer exhibits the highest $g_{\mathrm{eff}}^{\uparrow\downarrow}$ because the direct contact of CFGG with Pt facilitates efficient spin current transfer across the CFGG/Pt interface. The most pronounced decrease in α_{total} of ~ 22% (refer to Fig. 10(c)) is noted in the case of the Cu insertion layer. Such behavior of Cu insertion has been reported in the previous studies [5], and has been ascribed to a reduction of proximity-induced magnetization in the Pt layer, resulting from the nonmagnetic property of the Cu insertion layer. This leads to the reduction in $g_{\mathrm{eff}}^{\uparrow\downarrow}$ by ~ 32%. On the other hand, no noticeable change in α_{total}, and consequently in $g_{\mathrm{eff}}^{\uparrow\downarrow}$, is observed in the sample with Ni insertion layer, presumably owing to its similarity in magnetic property to that of the CFGG layer. A direct contact between FM and the Pt layer enables the formation of proximity-induced magnetization in the Pt layer [11,32,33]. In the case of nonmagnetic Ru and Ta insertion layers, a relatively smaller reduction in $g_{\mathrm{eff}}^{\uparrow\downarrow}$ (~ 22%) is observed in comparison to the Cu insertion layer. This difference in $g_{\mathrm{eff}}^{\uparrow\downarrow}$ might originate from the interfacial enhancement of spin-orbit coupling resulting from direct contact of CFGG layer with a material possessing relatively high spin-orbit coupling, such as Ru and Ta [7,8]. This explain the large θ_{H} in the films with Ru and

Ta insertion as compared to the one with Cu insertion layer [34]. In the case of the Cr insertion layer, $g_{\mathrm{eff}}^{\uparrow\downarrow}$ decreased only slightly (~ 12%) despite its low atomic number. Previous studies on $Y_3Fe_5O_{12}$ (YIG)/NM bilayers by Du *et al*. [26] and Wang *et al*. [34] reported that Cr (~ 0.051) has a smaller θ_{H} than Ta (~ 0.071), although Cr shows a relatively high θ_{H} for its small atomic number due to its *d*-electron configuration. Therefore, $g_{\mathrm{eff}}^{\uparrow\downarrow}$ is expected to be lower for the Cr insertion layer compared to Ta when only θ_{H} of these materials is considered, which is contrary to the obtained result shown in Fig. 10(b). This discrepancy suggests that the antiferromagnetic property of the Cr insertion layer could increase the spin current transfer from CFGG to the Pt layer [35]. Based on the above discussion, it is apparent that the interfacial modification by ultrathin (~ 0.2 nm) insertion layers leads to a noticeable change in $g_{\mathrm{eff}}^{\uparrow\downarrow}$ while not affecting the structure of the Pt layer, highlighting the role of material characteristics at the interface on $g_{\mathrm{eff}}^{\uparrow\downarrow}$.

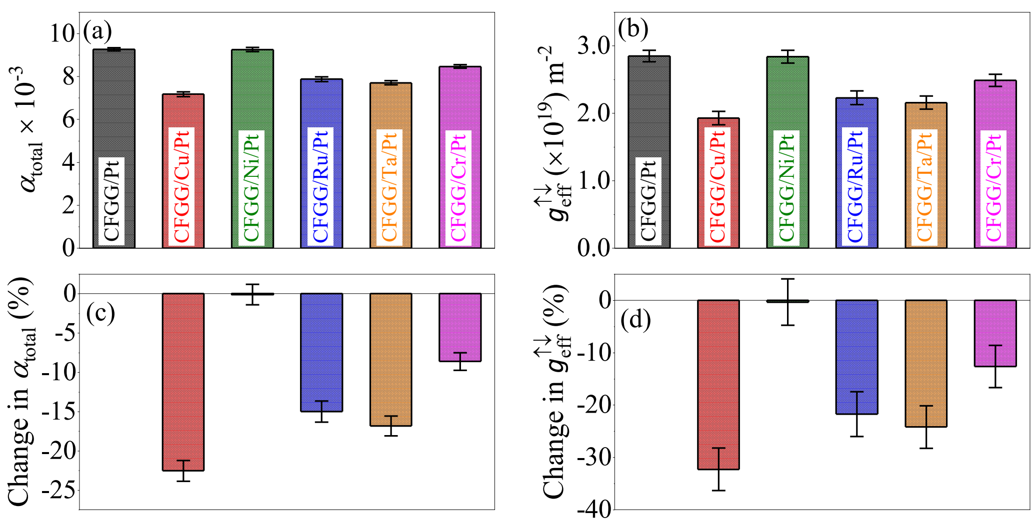

Fig. 10. (a) α_{total} and (b) $g_{\mathrm{eff}}^{\uparrow\downarrow}$ of bilayers without and with Cu, Ni, Ru, Ta, or Cr insertion layers. The percentage variation of the (c) α_{total} and (d) $g_{\mathrm{eff}}^{\uparrow\downarrow}$ for different insertion layers.

4. CONCLUSIONS

A high $g_{\mathrm{eff}}^{\uparrow\downarrow}$ at the FM/HM interface, along with low α in the FM, is essential for enabling faster and more energy-efficient spintronic devices. In this study, we evaluated $g_{\mathrm{eff}}^{\uparrow\downarrow}$ in CFGG/Pt bilayer thin films and the effects of different ultrathin (~ 0.2 nm) insertion layers using FMR measurements. The single-layer CFGG sample showed a low Gilbert damping of ~ 1.07×10^{-3}, while a notable increase, observed in CFGG/Pt bilayers, indicates efficient spin pumping across the interface, from which a high $g_{\mathrm{eff}}^{\uparrow\downarrow}$ of $(2.78\pm0.09)\times10^{19}$ m^{-2} was estimated. While investigating the effect of an insertion layer on $g_{\mathrm{eff}}^{\uparrow\downarrow}$, XRD and STEM measurements confirmed that the Pt structure remained largely unaffected by the insertion layers. This confirmation eliminates the possibility of the insertion-layer-induced changes in the Pt layer. The insertion of the NM Cu layer significantly reduces $g_{\mathrm{eff}}^{\uparrow\downarrow}$, while the FM Ni layer retains almost same $g_{\mathrm{eff}}^{\uparrow\downarrow}$. In the case of Ru and Ta insertion layers, despite being nonmagnetic, a slight reduction in $g_{\mathrm{eff}}^{\uparrow\downarrow}$ is observed, while the antiferromagnetic Cr insertion layer also causes a small decrease. The ultra-low Gilbert damping of CFGG, combined with high $g_{\mathrm{eff}}^{\uparrow\downarrow}$ in CFGG/Pt bilayers, highlights their potential for energy-efficient SOT induced magnetization switching in the active FM layer of magnetic tunnel junctions. Moreover, the effect of insertion layers provides insights into interface engineering for tuning $g_{\mathrm{eff}}^{\uparrow\downarrow}$. Future scope of the study includes elucidation of the microscopic mechanism underlying the influence of the insertion layer at the interface by employing theoretical analysis on α_{total} and $g_{\mathrm{eff}}^{\uparrow\downarrow}$ to obtain a deeper insight of the underlying physics.

Acknowledgement

This work is supported by the Advanced Storage Research Consortium (ASRC), JST CREST (Grant No. JPMJCR21O1), the MEXT Initiative to Establish Next-generation Novel Integrated Circuits Centers (X-NICS) (Grant No. JPJ011438), JST ERATO "Magnetic Thermal Management Materials Project" (Grant No. JPMJER2201). The authors thank Y. Miura and I. Kurniawan at NIMS for fruitful discussions, and S. Kuramochi and N. Kojima at NIMS for the preparation and characterization of thin films.

Data availability statement

The data that support the findings of this study are openly available in Materials Data Repository (MDR) operated by National Institute for Materials Science at https://doi.org/10.48505/nims.6269.

References

[1] S. Ikegawa, F. B. Mancoff, J. Janesky, and S. Aggarwal, Magnetoresistive Random Access Memory: Present and Future, IEEE Trans. Electron Devices **67**, 1407 (2020).

[2] K. Dolui, U. Bajpai, and B. K. Nikolić, Effective spin-mixing conductance of topological-insulator/ferromagnet and heavy-metal/ferromagnet spin-orbit-coupled interfaces: A first-principles Floquet-nonequilibrium Green function approach, Phys. Rev. Mater. **4**, 121201(R) (2020).

[3] Q. Lu, Y. Li, B. Peng, H. Tang, Y. Zhang, Z. He, L. Wang, C. Li, W. Su, Q. Yang, Z. Zhou, and M. Liu, Enhancement of the spin-mixing conductance in Co-Fe-B/W bilayers by interface engineering, Phys. Rev. Appl. **12**, 064035 (2019).

[4] S. Akansel, A. Kumar, N. Behera, S. Husain, R. Brucas, S. Chaudhary, and P. Svedlindh, Thickness-dependent enhancement of damping in Co_2FeAl/β-Ta thin films, Phys. Rev. B. **97**, 134421(2018).

[5] A. Kumar, R. Gupta, S. Husain, N. Behera, S. Hait, S. Chaudhary, R. Brucas, and P. Svedlindh, Spin pumping and spin torques in interfacially tailored Co_2FeAl/β-Ta layers, Phys. Rev. B. **100**, 214433 (2019).

[6] B. B. Singh, K. Roy, P. Gupta, T. Seki, K. Takanashi, and S. Bedanta, High spin mixing conductance and spin interface transparency at the interface of a $Co_2Fe_{0.4}Mn_{0.6}Si$ Heusler alloy and Pt, NPG Asia Mater. **13**(9), (2021).

[7] E. Barati, M. Cinal, D. M. Edwards, and A. Umerski, Gilbert damping in magnetic layered systems, Phys Rev B **90**, 014420 (2014).

[8] S. Azzawi, A. Ganguly, M. Tokaç, R. M. Rowan-Robinson, J. Sinha, A. T. Hindmarch, A. Barman, and D. Atkinson, Evolution of damping in ferromagnetic/nonmagnetic thin film bilayers as a function of nonmagnetic layer thickness, Phys Rev B **93**, 054402 (2016).

[9] Q. Zhang, S. I. Hikino, and S. Yunoki, First-principles study of the spin-mixing conductance in $Pt/Ni_{81}Fe_{19}$ junctions, Appl. Phys. Lett. **99**, 172105 (2011).

[10] M. Tokaç, S. A. Bunyaev, G. N. Kakazei, D. S. Schmool, D. Atkinson, and A. T. Hindmarch, Interfacial structure dependent spin mixing conductance in cobalt thin films, Phys. Rev. Lett. **115**, 056601 (2015).

[11] C. Swindells, H. Głowiński, Y. Choi, D. Haskel, P. P. Michałowski, T. Hase, P. Kuświk, and D. Atkinson, Proximity-induced magnetism and the enhancement of damping in ferromagnetic/heavy metal systems, Appl. Phys. Lett. **119**, 152401 (2021).

[12] C. Swindells, H. Glowinski, Y. Choi, D. Haskel, P. P. Michalowski, T. Hase, F. Stobiecki, P. Kuswik, and D. Atkinson, Magnetic damping in ferromagnetic/heavy-metal systems: The role of interfaces and the relation to proximity-induced magnetism, Phys. Rev. B **105**, 094433 (2022).

[13] Y. Fan, J. Wang, A. Chen, K. Yu, M. Zhu, Y. Han, S. Zhang, X. Lin, H. Zhou, X. Zhang and Q. Lin, Thickness-dependent Gilbert damping and soft magnetism in metal/Co-Fe-B/Metal Sandwich Structure, Nanomaterials **14**, 596 (2024).

[14] S. Mizukami, D. Watanabe, M. Oogane, Y. Ando, Y. Miura, M. Shirai, and T. Miyazaki, Low damping constant for Co_2FeAl Heusler alloy films and its correlation with density of states, J. Appl. Phys. **105**, 07D306 (2009).

[15] T. Kubota, S. Tsunegi, M. Oogane, S. Mizukami, T. Miyazaki, H. Naganuma, and Y. Ando, Half-metallicity and Gilbert damping constant in $Co_2Fe_xMn_{1-x}Si$ Heusler alloys depending on the film composition, Appl. Phys. Lett. **94**, 122504 (2009).

[16] M. M. Bhat, K. Simalaotao, H. Suto, A. Perumal, A. Srinivasan, and Y. Sakuraba, Atomic order induced reduction of Gilbert damping constant and enhancement of half-metallicity in off-stoichiometric $Co_2FeGa_{0.5}Ge_{0.5}$ Heusler alloy thin films, J. Appl. Phys. **138**, 043904 (2025).

[17] J. M. Shaw, E. K. Delczeg-Czirjak, E. R. J. Edwards, Y. Kvashnin, D. Thonig, Martin A. W. Schoen, M. Pufall, M. L. Schneider, T. J. Silva, O. Karis, K. P. Rice, O. Eriksson, and H. T. Nembach, Magnetic damping in sputter-deposited Co_2MnGe Heusler compounds with *A*2, *B*2, and $L2_1$ orders: Experiment and theory, Phys. Rev. B **97**, 094420 (2018).

[18] Y. K. Takahashi, A. Srinivasan, B. Varaprasad, A. Rajanikanth, N. Hase, T. M. Nakatani, S. Kasai, T. Furubayashi, and K. Hono, Large magnetoresistance in current-perpendicular-to-plane pseudospin valve using a $Co_2Fe(Ge_{0.5}Ga_{0.5})$ Heusler alloy, Appl. Phys. Lett. **98**, 152501 (2011).

[19] Y. Sakuraba, M. Ueda, Y. Miura, K. Sato, S. Bosu, K. Saito, M. Shirai, T. J. Konno, and K. Takanashi, Extensive study of giant magnetoresistance properties in half-metallic Co_2(Fe,Mn)Si-based devices, Appl. Phys. Lett. **101**, 252408 (2012).

[20] D. Taparia, T. Sasaki, T. Nakatani, H. Suto, Y. Miura, Z. Li, V. K. Kushwaha, K. Inubushi, S. Ichikawa, K. Nakada, T. Sasaki, S. Mitani and Y. Sakuraba, Improvement in CPP-GMR read head sensor performance using [001]-oriented polycrystalline half-metallic Heusler alloy $Co_2FeGa_{0.5}Ge_{0.5}$ and CoFe bilayer electrode, Sci. Technol. Adv. Mater. **25(1)**, 2388503 (2024).

[21] V. Barwal, H. Suto, R. Toyama, K. Simalaotao, T. Sasaki, Y. Miura, and Y. Sakuraba, Large magnetoresistance and high spin-transfer torque efficiency of $Co_2Mn_xFe_{1-x}Ge$ ($0 \leq x \leq 1$) Heusler alloy thin films obtained by high-throughput compositional optimization using combinatorially sputtered composition-gradient film, APL Mater. **12**, 111114 (2024).

[22] S. Li, Y. K. Takahashi, T. Furubayashi, and K. Hono, Enhancement of giant magnetoresistance by $L2_1$ ordering in $Co_2Fe(Ge_{0.5}Ga_{0.5})$ Heusler alloy current-perpendicular-to-plane pseudo spin valves, Appl. Phys. Lett. **103**, 042405 (2013).

[23] J. W. Jung, Y. Sakuraba, T. T. Sasaki, Y. Miura, and K. Hono, Enhancement of magnetoresistance by inserting thin NiAl layers at the interfaces in $Co_2FeGa_{0.5}Ge_{0.5}$/Ag/$Co_2FeGa_{0.5}Ge_{0.5}$ current-perpendicular-to-plane pseudo spin valves, Appl. Phys. Lett. **108**, (2016).

[24] B. S. D. C. S. Varaprasad, A. Srinivasan, Y. K. Takahashi, M. Hayashi, A. Rajanikanth, and K. Hono, Spin polarization and Gilbert damping of $Co_2Fe(Ga_xGe_{1-x})$ Heusler alloys, Acta Mater. **60**, 6257 (2012).

[25] Y. Tserkovnyak, A. Brataas, and G. E. W. Bauer, Enhanced Gilbert damping in thin ferromagnetic films, Phys. Rev. Lett. **88**, 4 117601 (2002).

[26] C. Du, H. Wang, F. Yang, and P. C. Hammel, Systematic variation of spin-orbit coupling with *d*-orbital filling: Large inverse spin Hall effect in 3*d* transition metals, Phys. Rev. B **90**, 140407(R) (2014).

[27] S. Hait, S. Husain, V. Barwal, N. K. Gupta, L. Pandey, P. Svedlindh, and S. Chaudhary, Comparison of high temperature growth versus post-deposition in situ annealing in attaining very low Gilbert damping in sputtered Co_2FeAl Heusler alloy films, J. Magn. Magn. Mater. **519**, 167509 (2021).

[28] K. Goto, L. S. R. Kumara, Y. Sakuraba, Y. Miura, I. Kurniawan, A. Yasui, H. Tajiri, Y. Fujita, Z. Chen, and K. Hono, Effects of the atomic order on the half-metallic electronic structure in the $Co_2Fe(Ga_{0.5}Ge_{0.5})$ Heusler alloy thin film, Phys. Rev. Mater. **4**, 114406 (2020).

[29] X. Tao, Q. Liu, B. Miao, R. Yu, Z. Feng, L. Sun, B. You, J. Du, K. Chen, S. Zhang, L. Zhang, Z. Yuan, D. Wu, H. Ding, Self-Consistent determination of spin Hall angle and spin diffusion length in Pt and Pd: The Role of the Interface Spin Loss, Sci. Adv. **4**, 1670 (2018).

[30] T. Fache, J. C. Rojas-Sanchez, L. Badie, S. Mangin, and S. Petit-Watelot, Determination of spin Hall angle, spin mixing conductance, and spin diffusion length in CoFeB/Ir for spin-orbitronic devices, Phys. Rev. B. **102**, 064425 (2020).

[31] J. M. Shaw, H. T. Nembach, and T. J. Silva, Determination of spin pumping as a source of linewidth in sputtered $Co_{90}Fe_{10}$/Pd multilayers by use of broadband ferromagnetic resonance spectroscopy, Phys. Rev. B **85**, 054412 (2012).

[32] F. Wilhelm, P. Poulopoulos, G. Ceballos, H. Wende, K. Baberschke, P. Srivastava, D. Benea, H. Ebert, M. Angelakeris, N. K. Flevaris, D. Niarchos, A. Rogalev, and N. B. Brookes, Layer-resolved magnetic moments in Ni Pt multilayers, Phys. Rev. Lett., **85**, 413 (2000).

[33] M. Caminale, A. Ghosh, S. Auffret, U. Ebels, K. Ollefs, F. Wilhelm, A. Rogalev, and W. E. Bailey, Spin pumping damping and magnetic proximity effect in Pd and Pt spin-sink layers, Phys Rev B **94**, 014414 (2016).

[34] H. L. Wang, C. H. Du, Y. Pu, R. Adur, P. C. Hammel, and F. Y. Yang, Scaling of spin Hall angle in 3*d*, 4*d*, and 5*d* metals from $Y_3Fe_5O_{12}$/metal spin pumping, Phys. Rev. Lett. **112**, 197201 (2014).

[35] H. Wang, C. Du, P. C. Hammel, and F. Yang, Antiferromagnonic spin transport from $Y_3Fe_5O_{12}$ into NiO, Phys. Rev. Lett. **113**, 097202 (2014).